MATERIALS SCIENCE

Large spin-orbit torque efficiency enhanced by magnetic structure of collinear antiferromagnet IrMn

Jing Zhou[1], Xiao Wang[2], Yaohua Liu[3], Jihang Yu[1], Huixia Fu[4], Liang Liu[1], Shaohai Chen[1], Jinyu Deng[1], Weinan Lin[1], Xinyu Shu[1], Herng Yau Yoong[1], Tao Hong[3], Masaaki Matsuda[3], Ping Yang[1,5], Stefan Adams[1], Binghai Yan[4], Xiufeng Han[2], Jingsheng Chen[1,6]*

Spin-orbit torque (SOT) offers promising approaches to developing energy-efficient memory devices by electric switching of magnetization. Compared to other SOT materials, metallic antiferromagnet (AFM) potentially allows the control of SOT through its magnetic structure. Here, combining the results from neutron diffraction and spin-torque ferromagnetic resonance experiments, we show that the magnetic structure of epitaxially grown $L1_0$-IrMn (a collinear AFM) is distinct from the widely presumed bulk one. It consists of twin domains, with the spin axes orienting toward [111] and [−111], respectively. This unconventional magnetic structure is responsible for much larger SOT efficiencies up to 0.60 ± 0.04, compared to 0.083 ± 0.002 for the polycrystalline IrMn. Furthermore, we reveal that this magnetic structure induces a large isotropic bulk contribution and a comparable anisotropic interfacial contribution to the SOT efficiency. Our findings shed light on the critical roles of bulk and interfacial antiferromagnetism to SOT generated by metallic AFM.

INTRODUCTION

Spin-orbit torque (SOT) has been extensively investigated due to its application in the electric switching of magnetization (*1*–*5*). Magnetic memory based on SOT is considered to have higher speed and lower energy consumption than spin transfer torque magnetic random access memory (*6*, *7*). In a ferromagnetic/heavy metal (FM/HM) bilayer, SOT arises from the spin Hall effect (SHE) in HM (*1*, *2*) and/or the Rashba-Edelstein effect at the interface (*3*–*5*). In the case of SHE, a spin current generated from HM due to spin-orbit interaction is transferred to FM and exerts a spin transfer torque on the magnetic moment. The magnetization switching efficiency therefore depends substantially on the overall efficiency of SOT, which includes the charge-to-spin conversion efficiency and the transmission efficiency of spin current into the adjacent FM layer. To date, evidences of large SOT efficiency have been observed in topological insulators (*6*, *8*, *9*), HM (*10*–*14*), and metallic antiferromagnet (AFM) (*15*–*18*). These materials, in general, have strong bulk and/or interfacial spin-orbit coupling (SOC), which accounts for the intrinsic contribution to SOT.

Studies on SOT of metallic AFM, in addition, emphasize the roles of antiferromagnetism. In $L1_2$-$IrMn_3$, the triangular arrangement of magnetic moment within the (111) plane results in considerable spin Hall conductivity (SHC) in the [001] direction, which is associated with a facet-dependent SOT efficiency (*15*). Zhang *et al.* (*19*) demonstrate anisotropic SOT efficiency in $L1_0$-IrMn, which is attributed to the changed spin texture associated with different epitaxial growth directions, although the measured spin Hall angles (SHAs) are not notably different from those of polycrystalline IrMn. The interfacial exchange coupling in an AFM/FM bilayer has also been shown to influence the SOT efficiency (*15*–*17*, *20*). A higher SOT efficiency is observed in IrMn/FM with a larger exchange bias, but the direction of exchange bias appears to have little effect (*15*, *16*). Sometimes, conflicting results on the influence of exchange bias are also reported (*16*, *20*). The measured SOT efficiencies of IrMn are very scattered and range from 0.02 to 0.35 (*15*–*17*, *19*, *20*). These imply multiple, and perhaps conflicting, factors that may affect SOT of IrMn.

We perceive the above controversies as two related problems that have not been sufficiently addressed. First, the magnetic structure of IrMn is not defined while probing its SOT. Ideally, IrMn can exist in three forms with distinct crystallographic and magnetic structures, namely, the γ, $L1_0$, and $L1_2$ phases (*17*, *21*). In practice, the strength of SOT of IrMn is substantially lowered due to the averaging effect of randomly oriented crystallites and domains (*17*). The effects from substrate, such as epitaxial strain, further complicate this. The assumption of magnetic structure based on merely atomic composition or crystal structure is therefore weak. Second, the interfacial contribution to SOT from the IrMn/FM bilayer is not well separated from the bulk contribution. Previous studies frequently use field cooling (after annealing) to tune the magnetic structure of the IrMn/FM bilayer (*15*, *20*). This technique results in the simultaneous changes in the bulk and/or interfacial magnetic orders in AFM, the degree of crystallization in both layers, as well as interfacial mixing, all of which influence the measured SOT efficiency. Moreover, the magnetic damping constant of the FM in the exchange-biased AFM/FM bilayer is usually enhanced (*16*, *20*). This frustrates the initiatives of energy-efficient memory, where a small damping constant is favored (*6*). Although field-free switching of magnetization using SOT and exchange bias has been realized in IrMn/CoFeB (*5*), the identification of useful sources of SOTs in IrMn and the effective ways to engineer them remain elusive.

Here, we report the epitaxial growth of the $L1_0$-IrMn (001) thin film of well-defined crystal and magnetic structures. Neutron diffraction measurement shows that the antiparallel Mn spin moments in our $L1_0$-IrMn tilt away from the crystallographic *c* axis by 56° ± 8°, which is different from bulk $L1_0$-type AFM (*17*, *22*–*24*). The measured SOT efficiency in $L1_0$-IrMn/$Ni_{81}Fe_{19}$ [also known as permalloy (Py)] reaches up to 0.60 ± 0.04 and displays a fourfold anisotropy. This anisotropy coincides closely with the two types of domains in $L1_0$-IrMn,

[1]Materials Science & Engineering, National University of Singapore, 9 Engineering Drive 1, Singapore 117575, Singapore. [2]Institute of Physics and Beijing National Laboratory for Condensed Matter Physics, Chinese Academy of Sciences, Beijing, China. [3]Neutron Scattering Division, Oak Ridge National Laboratory, Oak Ridge, TN, USA. [4]Department of Condensed Matter Physics, Weizmann Institute of Science, Rehovot, Israel. [5]Singapore Synchrotron Light Source (SSLS), National University of Singapore, 5 Research Link, Singapore 117603, Singapore. [6]Suzhou Research Institute, National University of Singapore, Suzhou 215123, China.
*Corresponding author. Email: msecj@nus.edu.sg

which align with [111] and [−111], respectively. After breaking the interfacial exchange coupling with a Cu spacer, the SOT efficiency drops substantially to 0.22 ± 0.03, and the fourfold anisotropy vanishes completely. Our results suggest that, in addition to a large bulk component of SOT efficiency in $L1_0$-IrMn, a comparable interfacial contribution dependent on the magnetic structure exists. By passing electric current along different crystal directions of $L1_0$-IrMn in a $L1_0$-IrMn/Py bilayer, the strength of current-induced SOT can be controlled.

RESULTS

Thin films in the stacking of IrMn/Py are deposited on $KTaO_3$ (001) substrates. See more details in Materials and Methods. Figure 1B shows a representative θ-2θ x-ray diffraction (XRD) pattern of the IrMn film. The presence of all peaks in the (001) family and the absence of the (200) peak indicate a high degree of (001) texture. It also rules out the presence of the γ phase, which would show only a (002) peak at 48° due to the face-centered cubic (FCC) crystal structure (*21*). With Rietveld whole powder pattern fitting of the XRD measurements using the General Structure Analysis System (GSAS) software suite (*25*), the occupancy of Mn on the Ir site and vice versa is estimated to be (8 ± 2)%, which corresponds to a chemical ordering of S_{IrMn} = 0.84 ± 0.04. Figure 1 (C and D) shows the reciprocal space mappings (RSMs) of (103) and (113) planes, respectively. The presence of the (113) peak and the absence of the (103) peak are consistent with the characteristic selection rules of the $L1_0$ superlattice, where the sum of $h + k$ = even. The RSMs also rule out the existence of $L1_2$-$IrMn_3$ due to the absence of the (103) peak. The lattice constants determined from the (113) RSMs are $a = b = 3.868 \pm 0.004$ Å and $c = 3.638 \pm 0.001$ Å ($c/a = 0.941$). The lattice constant a in our films is slightly larger than the bulk value (3.855 Å), while the lattice constant c is slightly smaller than the bulk value (3.644 Å) (*17*). These findings can be attributed to the tensile strain from the lattice mismatch with the $KaTiO_3$ (001) substrate (a = 3.989 Å), which stretches a and compresses c. Similar results have been observed in $L1_0$-FePt films, where it is also found that an appropriate strain will favored the formation of the $L1_0$ structure (*26*). The microstructure of the IrMn film is examined using high-resolution transmission electron microscopy (HRTEM), as shown in Fig. 1E. The IrMn film grows epitaxially on the $KTaO_3$ (001) substrate. The reciprocal lattices at the substrate, film, and interface are similar except that the (01 L) family is missing for IrMn, consistent with the selection rule for the $L1_0$ phase.

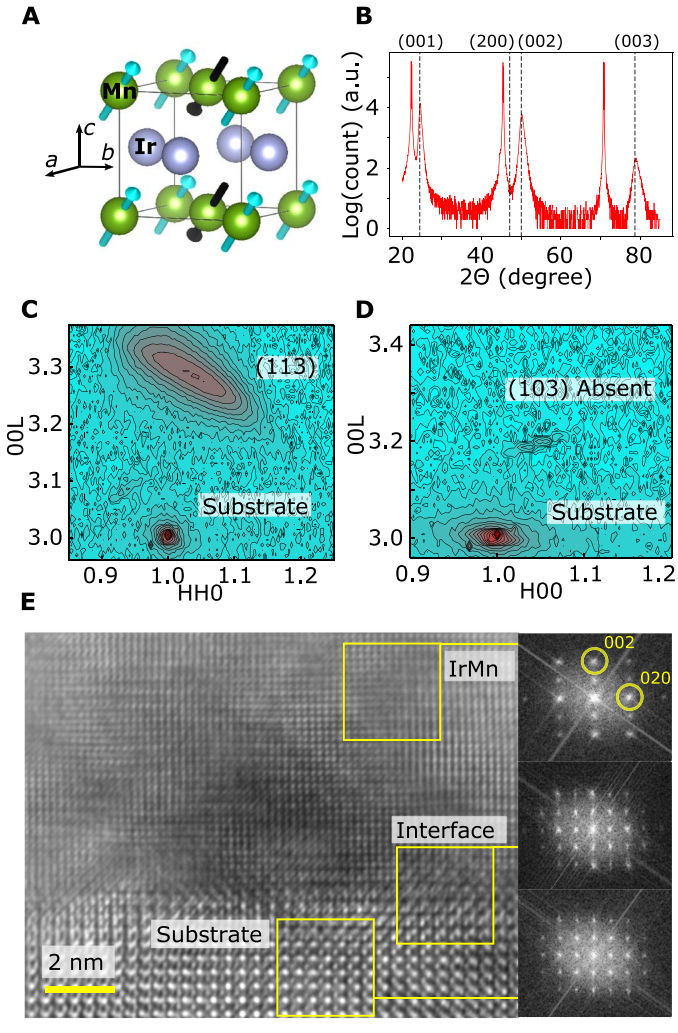

Fig. 1. Structure of $L1_0$-IrMn. (**A**) Schematic drawing of $L1_0$-IrMn unit cell. (**B**) XRD θ-2θ scan of IrMn along the (001) direction. Dotted lines show the reference peak positions of bulk $L1_0$-IrMn. a.u., arbitrary units. (**C** and **D**) RSMs around (113) and (103) planes, respectively. (**E**) HRTEM image of cross section of $L1_0$-IrMn thin film. Diffraction patterns from the substrate, interface, and IrMn are shown on the right.

Then, we use neutron diffraction to investigate the magnetic structure of the IrMn (001) film. Figure 2 shows the θ-2θ scans in selected directions. The lattice constants determined from the θ-2θ scan are $a = b = 3.900 \pm 0.004$ Å and $c = 3.644 \pm 0.001$ Å ($c/a = 0.934$), which are similar to the XRD results shown above. For the single-crystal thin film, the integrated intensity can be expressed by $< I_{hkl} > = \frac{A<q^2> F^2_{mag}}{\sin(2\theta)}$ (*22*, *23*), where A is a constant and F^2_{mag} is the magnetic structure factor. $<q^2>$ is the projection factor describing the component of magnetic moment perpendicular to the [*hkl*] direction. In the case of tetragonal symmetry, it can be expressed as (*23*)

$$< q^2 > = 1 - \frac{l^2 + \left[\frac{1}{2}\left(\frac{c}{a}\right)^2 (h^2 + k^2) - l^2\right] \sin^2(\psi_c)}{\left(\frac{c}{a}\right)^2 (h^2 + k^2) + l^2} \quad (1)$$

Here, ψ_c is the angle between the magnetic moment and the [001] direction. Assuming no magnetic moment on Ir atom and a collinear arrangement of magnetic moment on Mn, ψ_c can be evaluated from the ratio $R = \frac{<I_{100}>}{<I_{101}>}$. The measured R is 1.64 ± 0.26, which is equivalent to a 56° ± 8° (Fig. 1A) tilting angle with the c axis (see Supplementary Materials and Methods). The in-plane orientation of the magnetic moment cannot be determined from neutron diffraction due to the tetragonal symmetry of the $L1_0$ phase (*22*–*24*). Theoretical calculations on $L1_0$-type AFMs predict that the staggered magnetic moments on Mn are either parallel or perpendicular to the [001] direction (*22*, *23*), which correspond to R being 3.58 or 1.09, respectively, in perfectly ordered $L1_0$-IrMn. Thus, taking the error bar in measured R into account, our $L1_0$-IrMn is still considered to exhibit spin canting, which might be possibly due to the small strain induced from the lattice mismatch with the substrate (*24*). In addition, the existence of small chemical disorder might also influence the alignment of magnetic moments.

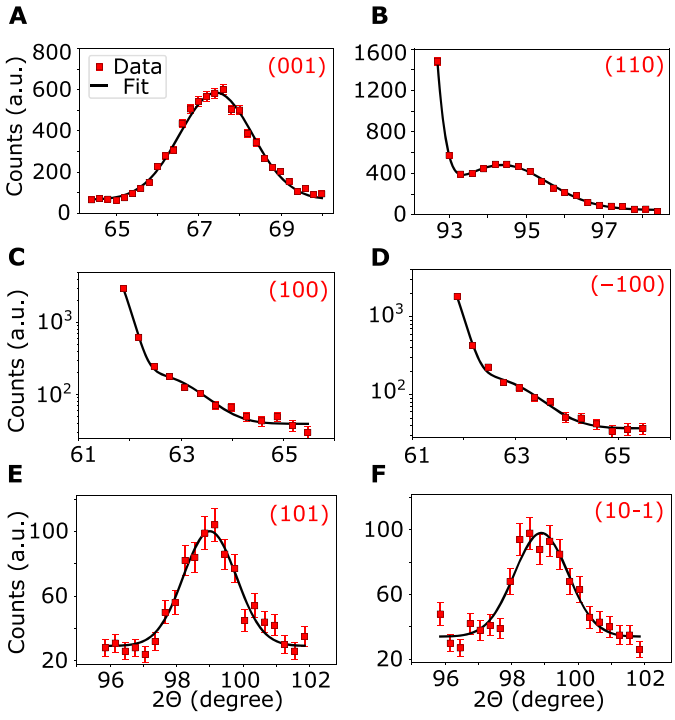

Fig. 2. Neutron diffraction θ-2θ scans along different directions. (**A**) (001). (**B**) (110). (**C**) (100). (**D**) (−100). (**E**) (101). (**F**) (10-1).

The estimated magnetic moment is 3.54 ± 0.27 μ_B per Mn atom by comparing the integrated peak intensities of the magnetic peaks and the nuclear peaks, which is comparable to previous work (*22*, *23*).

We use the spin torque ferromagnetic resonance (ST-FMR) technique (*10*, *15*, *20*, *27*) to evaluate the SOT efficiency of $L1_0$-IrMn in a $L1_0$-IrMn (d_{AF})/Py (d_F) bilayer (see Supplementary Materials and Methods). d_{AF} and d_F are the thicknesses of the IrMn and Py in nanometers, respectively. The stacking is patterned into the microstrip by photolithography and ion milling. A microwave is applied to the microstrip, while an external magnetic field (H) in the sample plane is swept at 45° with respect to the microstrip, as illustrated in Fig. 3A. While precessing, the magnetic moment in the Py layer experiences a field-like torque (τ_{FL}) and a damping-like torque (τ_{DL}). In the original ST-FMR model on Pt/Py (*27*), the Oersted field (h_{oe}) of microwave is considered to be the only contribution to τ_{FL}, while τ_{DL} is mainly caused by spin current (J_s) converted from charge current (J_c) flowing in the Pt (IrMn in our case) layer due to SHE. The precession of the magnetic moment leads to an anisotropic magnetoresistance effect in Py. This, when mixing with the alternating current, produces a rectifying DC voltage V_{mix} (zeroth harmonic) over the microstrip. As shown in Fig. 3C, V_{mix} can be decomposed into a symmetric component (S), which is associated with τ_{DL}, and into an antisymmetric component (A), which corresponds to τ_{FL}. Thus, the SOT efficiency is expressed as $\theta_{DL,m} = \frac{S}{A}\frac{e\mu_0 M_s d_{AF} d_F}{\hbar}\sqrt{1+\frac{4\pi M_{eff}}{H_{res}}}$ (*10*, *15*, *20*, *27*). Here, M_s and M_{eff} are the saturation magnetization and effective in-plane magnetization of the Py layer; H_{res} is the resonant field. In the absence of other sources of SOTs under the drift-diffusion model, the SOT efficiency here represents the overall charge-to-spin conversion efficiency and describes the lower bound of a traditional SHA, considering the losses of spin current density at the interface. As we shall discuss later, when additional SOTs are generated from other than bulk SHE of IrMn and Oersted field (*6*, *28*, *29*), the SOT efficiency from ST-FMR is merely the strength of τ_{DL} relative to τ_{FL}. Therefore, to avoid misleading notations, we use $\theta_{DL,m}$ to represent the measured damping-like SOT efficiency.

Typical ST-FMR voltage-frequency spectra, fitting of voltage, and resonant fields are shown in Fig. 3 (B to D), respectively. In Fig. 3E, $\theta_{DL,m}$ shows negligible dependence on measurement frequency. We find that the $\theta_{DL,m}$ (average of 8 to 12 GHz) of $L1_0$-IrMn is 0.59 ± 0.02, which is about an order of magnitude larger than its polycrystalline counterpart (p-IrMn) ($\theta_{DL,m}$ = 0.083 ± 0.002) and Pt ($\theta_{DL,m}$ = 0.061 ± 0.002). Similar values of $\theta_{DL,m}$ are found for other combinations of d_F and d_{AF} (fig. S4). This large $\theta_{DL,m}$ differs notably from those found previously in IrMn (*15*–*17*, *19*, *20*). Two approaches are taken to investigate the possible reasons.

To remove the effects of exchange coupling, we insert a thin Cu spacer between $L1_0$-IrMn and Py. Using the broadband FMR technique (*30*), we demonstrate the effect of Cu spacer in fig. S5A. In particular, 0.5 nm of Cu partially breaks the magnetically coupled IrMn and Py. Thicker Cu spacer results in complete magnetic separation of IrMn and Py, leading to a saturated damping constant (α). In Fig. 4A, $\theta_{DL,m}$ at 9 GHz drops markedly from 0.60 ± 0.04 for no Cu to 0.31 ± 0.02 for 0.5-nm Cu spacer and further to 0.22 ± 0.03 for 1-nm Cu spacer. Considering a partial decoupling of IrMn and Py with 0.5-nm Cu and the possible shunting with 1-nm Cu (see Supplementary Materials and Methods for estimation of shunting), the contribution to $\theta_{DL,m}$ from bulk $L1_0$-IrMn should be between 0.31 ± 0.02 and 0.22 ± 0.03 and the remaining has an interfacial origin. The strong effects of the interface can also be seen from Fig. 4B, where the exchange coupling results in enhancement in both ST-FMR linewidth (ΔH) and α. Even with the lower bound of $\theta_{DL,m}$ = 0.22 ± 0.03, bulk $L1_0$-IrMn still exhibits a large SOT efficiency, while α of the Py layer is less than 0.01. Such a combination of $\theta_{DL,m}$ and α is more compatible with designing energy-efficient magnetic memory, in contrast to bilayers with exchange bias (*16*, *20*).

Second, we fabricate ST-FMR devices with different in-plane orientations relative to the [100] direction of the $L1_0$-IrMn lattice on the same sample of $L1_0$-IrMn (22)/Py (13), as illustrated schematically in Fig. 5A. We find that $\theta_{DL,m}$ depends strongly on the device direction: $\theta_{DL,m}$ at 9 GHz is 0.60 ± 0.04 for the 45°-oriented device, while it is only 0.42 ± 0.04 for the 0° case (Fig. 4C). Unlike the case of Cu spacer, α does not change notably, although ΔH changes with device orientation (Fig. 4D). The ΔH values for the 0° (and 90°, 180°, 270° later) device are too large; thus, they are scattered at higher frequencies, in which a linear fit for α is less statistically robust. Nonetheless, for all other angles, α shows little dependence on the device orientation (fig. S5B). This is perhaps expected as the factors affecting α, such as the lateral distribution of domains and internal field (*30*, *31*), spin pumping (*32*, *33*), and exchange coupling (*16*, *17*, *20*), are essentially the same for the same sample.

We extend our investigation on the in-plane angle dependence of $\theta_{DL,m}$ in Fig. 4C to a full circle and other samples. $\theta_{DL,m}$ and H_{res} at 9 GHz are normalized and summarized in Fig. 5 (see fig. S6 for absolute values). In Fig. 5D, an anisotropic $\theta_{DL,m}$ of fourfold symmetry is observed for $L1_0$-IrMn (22)/Py (13). Similar results can be also observed in $L1_0$-IrMn (12)/Py (13). Replacing $L1_0$-IrMn with p-IrMn (Fig. 5B) or adding a Cu spacer (Fig. 5F) results in the loss of anisotropy. These indicate that the bulk component of $\theta_{DL,m}$ for $L1_0$-IrMn is isotropic. In contrast, its interfacial component is anisotropic and it is induced by the magnetic structure of the $L1_0$ phase. H_{res} in Fig. 5 (C, E, and G) shares the same symmetry of the respective $\theta_{DL,m}$. In Fig. 5E, a smaller H_{res} signals a larger internal field such that less external field is needed for

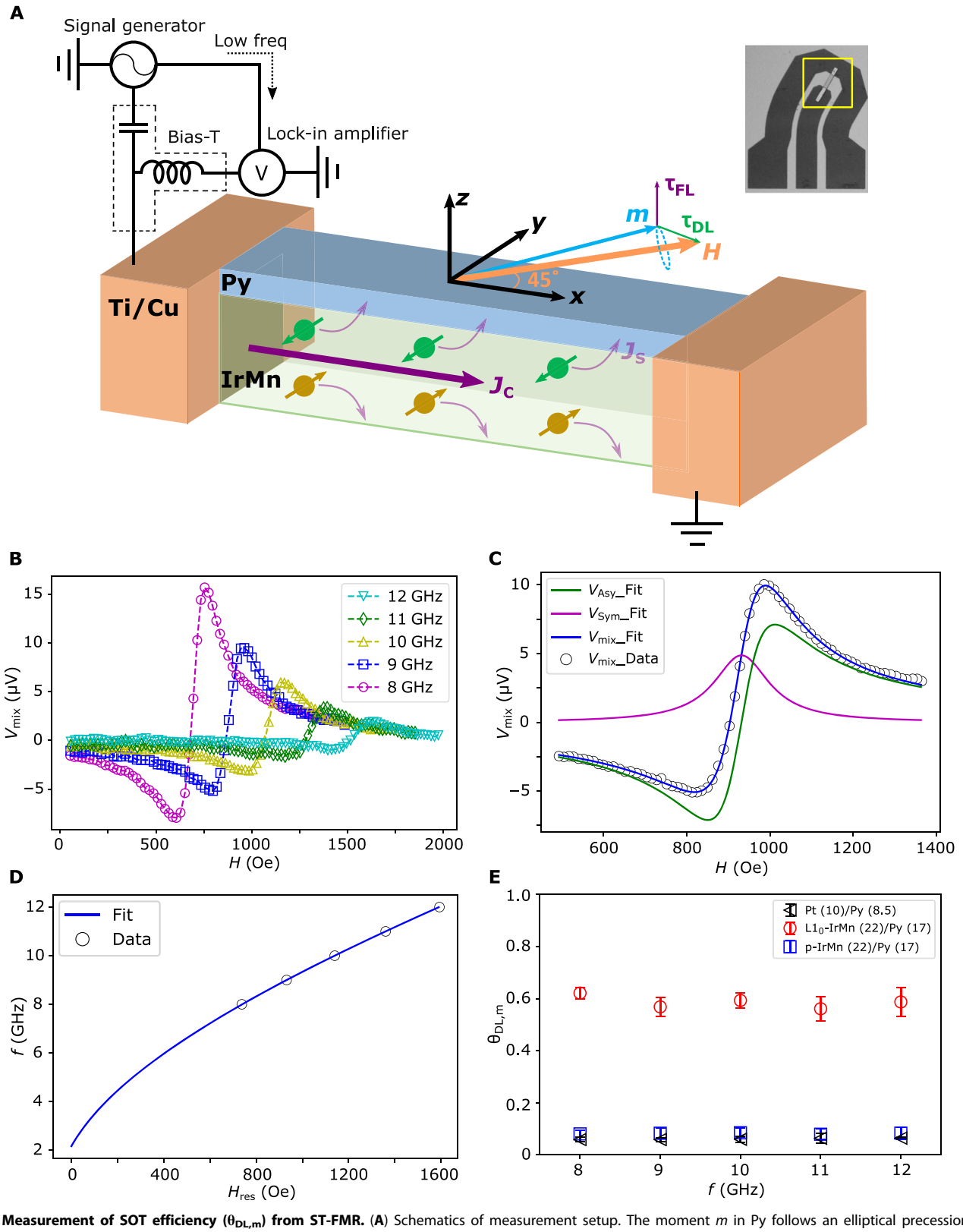

Fig. 3. Measurement of SOT efficiency ($\theta_{DL,m}$) from ST-FMR. (**A**) Schematics of measurement setup. The moment *m* in Py follows an elliptical precession route around the direction of *H*. It is influenced by two orthogonal torques τ_{FL} and τ_{DL}. Top right shows the optical image of the device and electrode (dark color). (**B**) Voltage spectra of $L1_0$-IrMn (22)/Py (17) measured from 8 to 12 GHz with nominal input power of 18 dBm. (**C**) Typical fitting of V_{mix} at 9 GHz. V_{sym} and V_{asym} correspond to the symmetric and antisymmetric components, respectively. (**D**) Fitting of Kittel equation. (**E**) $\theta_{DL,m}$ of $L1_0$-IrMn, p-IrMn, and Pt. The error bar describes 1 SD over at least five devices.

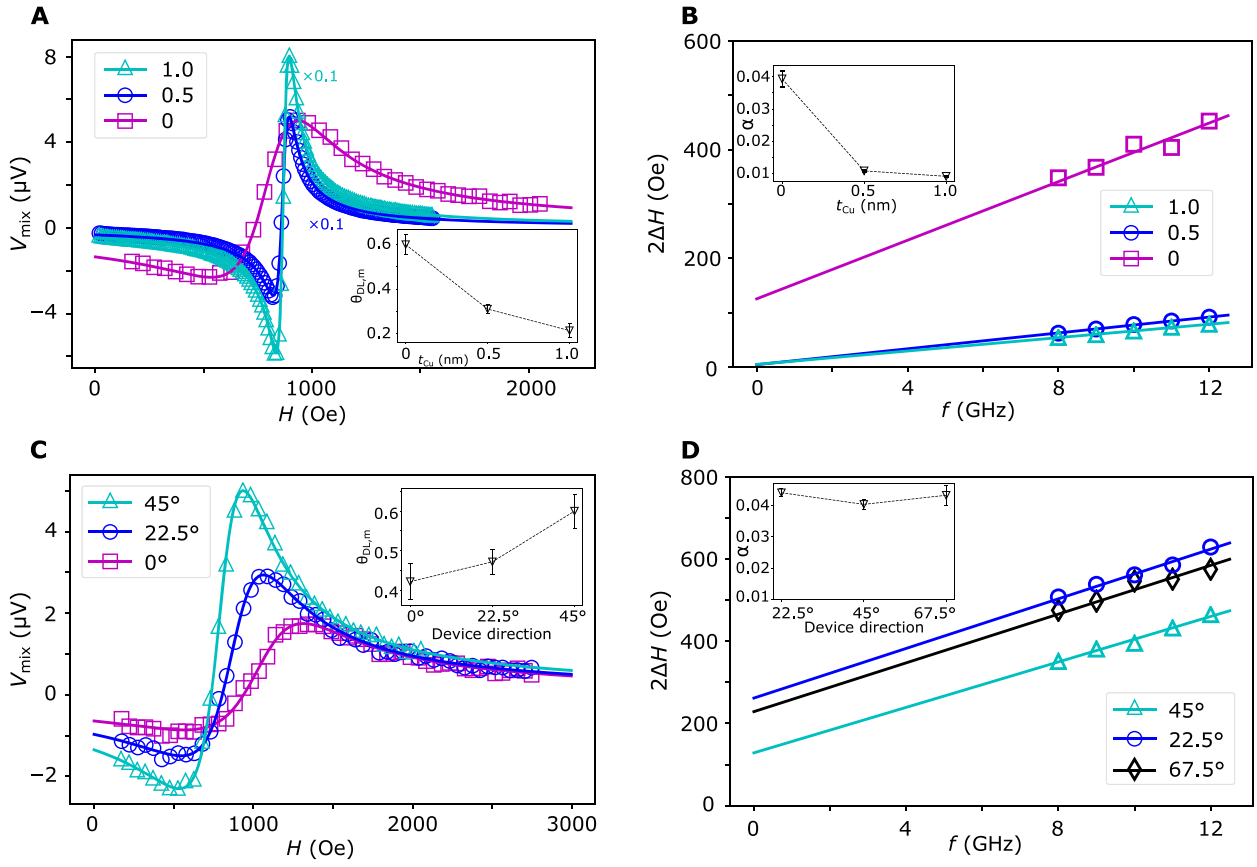

Fig. 4. Effect of Cu spacer and current direction on SOT efficiency ($\theta_{DL,m}$) in $L1_0$-IrMn. (**A**) V_{mix} (data point) and its fit (line) of $L1_0$-IrMn (22)/Cu (0, 0.5, 1)/Py (13) at 9 GHz. The voltage spectrum is scaled for a clearer comparison. (**C**) V_{mix} (data point) and its fit (line) of devices on $L1_0$-IrMn (22)/Py (13) at 9 GHz. The angle refers to the orientation of the microstrip in the film plane relative to the [100] direction of the $L1_0$-IrMn lattice. The insets of (A) and (C) show the extracted $\theta_{DL,m}$. (**B** and **D**) Linear fit of linewidths against frequency for devices in (A) and (C), respectively. Inset shows the extracted damping constant (α). The plot of the 0° device is too scattered and is therefore replaced by the 67.5° device in (D).

the resonance. It is worth noting that H is always at 45° with the microstrip during measurement (Fig. 3A). Thus, the two easy axes of magnetic anisotropy in Py are oriented along [100] (0°) and [010] (90°) of the $L1_0$-IrMn lattice, respectively. When a polycrystalline FM is exchange-coupled with a single-crystal AFM with an ordered magnetic structure, a fourfold magnetic anisotropy in FM can be induced by the magnetic anisotropy of AFM (*34*, *35*). More specifically, a collinear AFM with orthogonal domains, such as twined MnF_2 (110), induces two orthogonal uniaxial anisotropies in the FM film plane. The two uniaxial terms ultimately cancel each other, leaving a fourfold residue at 45° with AFM easy axes (*35*), as schematically shown in Fig. 6A. The bilayer of $L1_0$-IrMn/Py is highly consistent with the above scenario, implying two types of antiferromagnetic domains in $L1_0$-IrMn, whose in-plane projections align with [110] (45°) and [−110] (135°), respectively (Fig. 6B). Given the measured $\psi_c = 56^\circ \pm 8^\circ$ and the fact that the angle between [001] and [111] is 54.7°, our $L1_0$-IrMn thin films are likely to consist of two domains parallel to [111] and [−111]. In addition, the exchange bias field in the bilayer is relatively small since the two values of H_{res} on any measured axis are roughly identical. This is expected based on our fabrication process, where no bias field during growth or post-field annealing is applied. Overall, the results in Fig. 5 confirm an ordered twin-domain spin texture at the $L1_0$-IrMn/Py interface, which induces both the anisotropic $\theta_{DL,m}$ of $L1_0$-IrMn and the magnetic anisotropy of Py.

DISCUSSION

The large $\theta_{DL,m}$ in our $L1_0$-IrMn is rationalized from the following perspectives. We evaluate the intrinsic SHC by ab initio Berry phase calculations based on the band structure and wave functions of the pure $L1_0$-IrMn single crystal without any disorders (see Supplementary Materials and Methods). The intrinsic SHC depends on the electric current direction relative to the spin direction. It would exhibit a twofold in-plane anisotropy only for the case of a single domain (fig. S7). Vector sum of twin domains with orthogonal in-plane projections results in an isotropic bulk contribution to $\theta_{DL,m}$. This is consistent with Fig. 5F. The gap between $\theta_{DL,m}$ of $L1_0$-IrMn and p-IrMn is likely to be a result of differed crystal and magnetic structures. In p-IrMn, both the crystallites and magnetic domains are randomly oriented, leading to an averaged SHC substantially smaller than the case of single crystal and single domain (*17*). The measured SHC (>2500$\frac{\hbar}{e}\frac{S}{cm}$) (Supplementary Materials and Methods), though much larger than the simulated intrinsic one (<200 $\frac{\hbar}{e}\frac{S}{cm}$), is in the same order of magnitude as the experimentally obtained SHC in other works (*15*). A previous study has observed a similar gap between measured and simulated SHC, which is rationalized by the extrinsic contribution to SHE (*15*). Since our $L1_0$-IrMn is not fully chemically ordered with a small amount of Ir atoms wrongly occupying Mn position and vice versa, the small chemical disorder may be treated as impurities, which enhance the skew scattering (*6*, *13*, *14*) and thus an extrinsic contribution to $\theta_{DL,m}$.

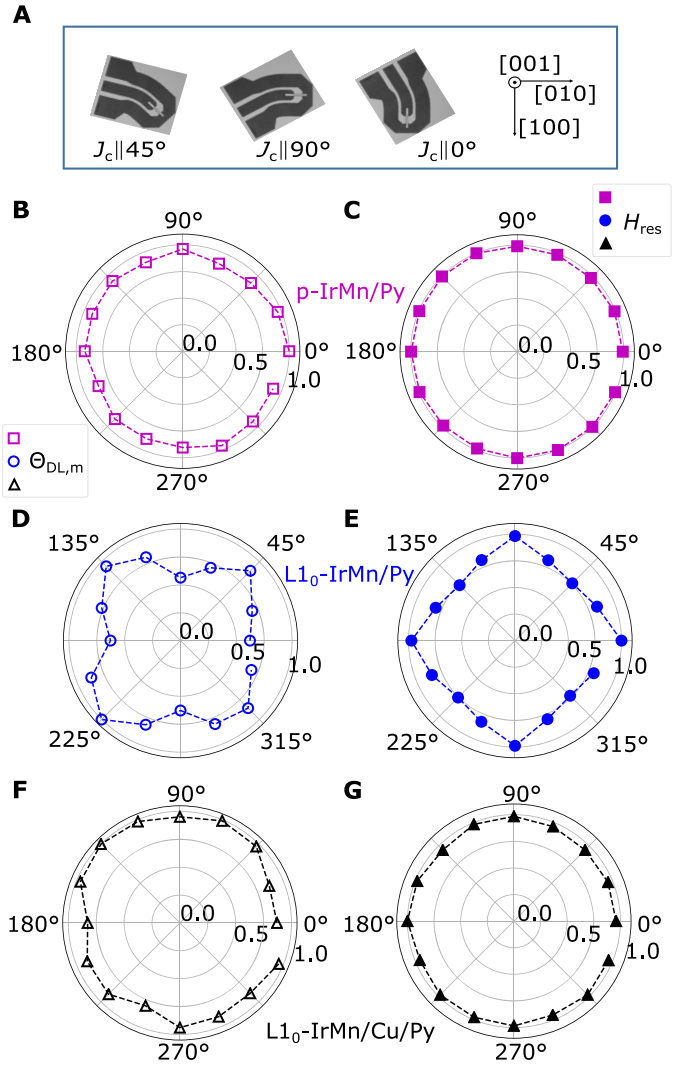

Fig. 5. In-plane angle dependence of SOT efficiency ($\theta_{DL,m}$) and resonance condition (H_{res}). (**A**) Schematic illustration of device orientation. The blue rectangle illustrates that multiple devices are patterned from the same continuous film. (**B**, **D**, and **F**) Normalized $\theta_{DL,m}$ at 9 GHz of p-IrMn (22)/Py (13), $L1_0$-IrMn (22)/Py (13), and $L1_0$-IrMn (22)/Cu (0.5)/Py (13), respectively. (**C**, **E**, and **G**) Normalized resonant fields (H_{res}) at 9 GHz of devices in (B), (D), and (F) respectively. The angle refers to the orientation of the microstrip in the film plane relative to the [100] direction for $L1_0$-IrMn samples and an arbitrary axis for the p-IrMn sample.

As reported by numerous authors, the electrical resistivity of the spin Hall layer can affect $\theta_{DL,m}$ (*6*, *11*, *12*). We measure the electrical resistivity of single-layer $L1_0$-IrMn and the electrical resistance of the bilayer microstrip. Both show little dependence on the device orientation (fig. S8).

Therefore, even in a highly ordered $L1_0$-IrMn with well-defined crystal (S_{IrMn}) and magnetic (ψ_c) structures, $\theta_{DL,m}$ cannot be explained fully on a bulk basis. We attempt to consider the anisotropic interfacial contribution to $\theta_{DL,m}$ in the drift-diffusion model plus interfacial spin-mixing conductance (*10*, *28*, *29*, *36*). That is, an isotropic spin current (and thus isotropic τ_{DL}, as in Fig. 5F) is generated from bulk $L1_0$-IrMn due to SHE and scattered anisotropically at the interface. The transparency due to electronic band mismatch (*10*, *36*), spin memory loss due to disorder (*36*, *37*) and SOC (*10*, *37*), and spurious voltage signal due to spin pumping and inverse spin Hall effect (ISHE) are likely to be independent of device orientation. The spin-dependent scattering, such as those analogous to the spin Hall magnetoresistance (SMR) effect (*38*), exhibits a fourfold ($\cos^2 x$ dependence) symmetry with the spin direction, and would be averaged because of twin-domain spin texture at the interface. Furthermore, all contributing factors above, except for ISHE, result in smaller $\theta_{DL,m}$ instead of an enhancement observed in this work.

The incompatibility of the model above implies the possibility of SOTs generated at the interface. As discussed by Kim *et al.* (*28*) and Haney *et al.* (*29*), considering a three-dimensional (3D) Rashba model with strong interfacial SOC, large τ_{DL} and τ_{FL} of comparable magnitudes can be generated from the interface. In the context of collinear AFM, the interface can be considered in a 2D Rashba model where inversion asymmetry exists in each sublattice, leading to a net Néel-order SOT of τ_{DL} nature (*39*). These torques have a strong dependence on the spin axis direction, which points to the possibility of the fourfold anisotropic $\theta_{DL,m}$ observed in this work. Since $\theta_{DL,m}$ only reflects the fraction of τ_{DL}/τ_{FL}, $\theta_{DL,m} = 0.60 \pm 0.04$ does not necessarily indicate more τ_{DL} per unit electric current compared to $\theta_{DL,m} = 0.22 \pm 0.03$. Therefore, the technical significance of an observed large SOT efficiency in exchange-coupled AFM/FM bilayers should be treated with care for future experimental design and application.

Our work also provides new insights into some of the seemingly contradictory results in the past. We notice in (*16*) that the exchange bias field is induced by an external field during film deposition. In contrast, the exchange bias field in (*20*) is produced by field cooling (after annealing). These two techniques result in starkly different IrMn/Py interfaces. Annealing would suppress the interfacial SOT by reducing the inversion asymmetry, as discussed by Garello *et al.* (*3*). In addition, interfacial disorder enhanced by annealing would also reduce the bulk contribution. Thus, Saglam *et al.* (*20*) observed a slight reduction in SOT efficiency after Py is magnetically coupled with IrMn, whereas Tshitoyan *et al.* (*16*) reported a huge increment similar to our case.

In addition, the dependence of current-induced SOT on the crystal direction has been reported in WTe_2, where the authors control the magnitude of a novel damping-like SOT via the broken crystal symmetry of WTe_2 (*40*). The anisotropic SOT efficiency in our work, though of a different physical origin, shares a similar phenomenological behavior and technical significance.

We are grateful toward one reviewer for suggesting a harmonic Hall voltage measurement as an independent method of evaluating the SOT in $L1_0$-IrMn/Py. The results are consistent with the findings of ST-FMR (see Supplementary Materials and Methods).

In summary, we have demonstrated the critical roles of crystal and magnetic structures in determining the SOT efficiency of $L1_0$-IrMn, which were insufficiently addressed and sometimes ignored previously. The $L1_0$-IrMn thin films in this work have high chemical order and a twin-domain magnetic structure different from bulk $L1_0$-type AFM. These account for the large SOT efficiency of more than 0.22 ± 0.03 in bulk $L1_0$-IrMn, in contrast to the small $\theta_{DL,m}$ (0.083 ± 0.005) in p-IrMn. By measuring the in-plane angle dependence of the ST-FMR response, we find a substantial enhancement of SOT efficiency up to 0.60 ± 0.04 due to the spin texture of the $L1_0$-IrMn/Py interface. We stress that the fourfold anisotropies in $\theta_{DL,m}$ and the magnetic anisotropy of Py, though they highly

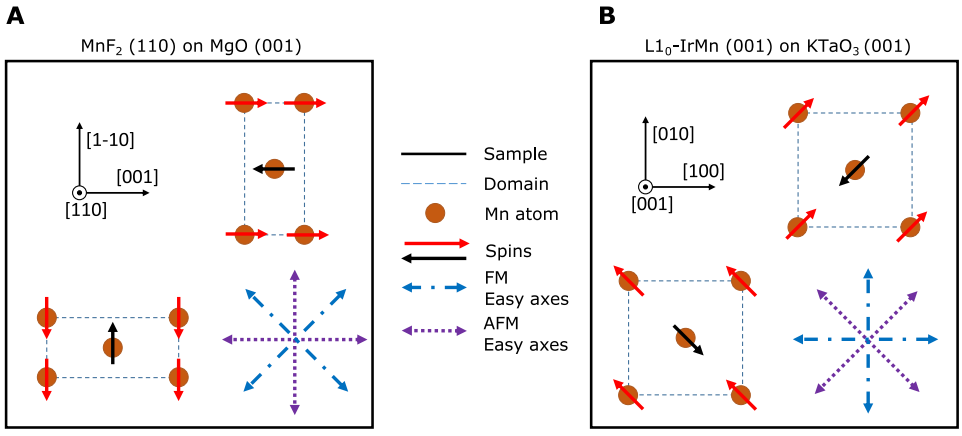

Fig. 6. Schematics of orthogonal domains in collinear AFM. (**A**) Twined MnF_2 (110) on MgO (001) according to (*35*). (**B**) $L1_0$-IrMn (001) on $KTaO_3$ (001) based on analysis of the magnetic anisotropy in exchange-coupled Py. The axes refer to the crystal lattice of the respective AFM film.

resemble each other, are not causal. Both are considered the results of $L1_0$-IrMn's magnetic structure.

MATERIALS AND METHOD

Thin-film deposition

Thin films were deposited by DC magnetron sputtering with a base pressure of less than 2×10^{-8} torr. In an attempt to produce high-quality $L1_0$-IrMn and to avoid problems with post-annealing, we deposited IrMn at elevated temperature. We tried a few substrates of small lattice mismatch, among which $L1_0$-IrMn of high chemical order and sufficiently smooth surface was produced only when the $KTaO_3$ substrate was used. Because of island growth at high temperature, $L1_0$-IrMn of less than 10 nm became discontinuous with high roughness and large electrical resistivity. Therefore, the thickness of our $L1_0$-IrMn was larger than past reports. In addition, considerable loss of Mn was observed at temperatures higher than 500°C, probably due to its high vapor pressure. Thus, our $L1_0$-IrMn was produced by first baking the $KTaO_3$ (001) substrate at 720°C for 30 min and then co-sputtering 5.08-cm $Ir_{40}Mn_{60}$ [atomic % (at %)] and Mn targets at the same temperature. Polycrystalline FCC IrMn as well as polycrystalline Py and Pt were deposited in situ at room temperature. All polycrystalline samples were deposited on the SiO_2 substrate. Because of strong exchange coupling between Py and $L1_0$-IrMn, Py of less than 10 nm exhibited a substantially larger coercive field and linewidth. The former introduced measurement artifacts in ST-FMR for smaller frequencies; the latter reduced the signal-to-noise ratio. Therefore, Py in this work was also thicker than past reports. A 2-nm SiO_2 was deposited by radio frequency (rf) magnetron sputtering on all samples as the protective layer. In this work, the nominal thicknesses of films were calibrated using an atomic force microscope. The real thicknesses were obtained from HRTEM, which were typically around 85% of the nominal ones. Thus, a nominal 25 nm became 22 nm and a nominal 15 nm became 13 nm, etc.

Material characterization

XRD (θ-2θ scan) and RSM were performed at room temperature in Singapore Synchrotron Light Source (SSLS) with an x-ray wavelength of 1.541 Å (Cu-Kα). Using Rutherford backscattering spectrometry, we found that epitaxial IrMn of a wide composition window (45 to 60 at % Mn) exhibited "$L1_0$-like" peaks from a simple θ-2θ scan. Therefore, we relied on RSM instead of composition to determine the phase and quality of IrMn, which were also verified by the magnetic property from neutron diffraction. HRTEM was performed using a JEOL 2010F field-emission microscope at a voltage of 200 kV. The sample was prepared by focused ion beam (FIB) technology through FEI versa 3D dual beam system and was next attached on an Omniprobe lift-out grid. Neutron diffraction was performed at room temperature in the θ–2θ mode with a neutron wavelength of 4.045 Å at the CG-4C at High Flux Isotope Reactor at Oak Ridge National Laboratory. The counts in Fig. 2 were fitted using a flat background plus one or two Gaussian functions, depending on whether there was an obvious contribution from the substrate.

Device fabrication

Devices for ST-FMR measurement were fabricated using a two-step method. First, the microstrip with a width of 10 to 30 μm and a length of 40 to 60 μm was patterned. We verified that different dimensions here did not affect the measured SHA. They only affected the resistance of the channel. Most of the data collected in this work were obtained using 30 μm × 50 μm devices. Second, the SiO_2 layer on the terminals of the microstrip was removed by etching before depositing the electrodes, which were typically Ti (5 nm)/Cu (100 nm). The electrode was deliberately bent in the clockwise direction, as shown in Figs. 3A and 5A, to match the position of rf probe in our system.

ST-FMR measurement

A Rohde & Schwarz SMB 100A signal generator was used to generate microwave with a frequency of 8 to 12 GHz and a nominal power of 18 dBm. We verified that power in the range of 10 to 18 dBm did not affect the measured SHA but only the signal-to-noise ratio. The ST-FMR measurement was modulated with a sine function to improve the signal-to-noise ratio. A nonmagnetic GSG three-terminal probe manufactured by GGB Industries Inc. was used to make electrical contact with the electrode. The probe was carefully rotated to ensure homogeneous contact. The modulated voltage output (V_{mix}) was collected using a Stanford Research SR830 lock-in amplifier.

SUPPLEMENTARY MATERIALS

Supplementary material for this article is available at http://advances.sciencemag.org/cgi/content/full/5/5/eaau6696/DC1

Supplementary Materials and Methods

Fig. S1. M-H loop of $L1_0$-IrMn/Py.

Fig. S2. Typical ST-FMR results of $L1_0$-IrMn (22)/Py (13) from 5 GHz to 12 GHz.

REFERENCES AND NOTES

1. S. Emori, U. Bauer, S.-M. Ahn, E. Martinez, G. S. D. Beach, Current-driven dynamics of chiral ferromagnetic domain walls. *Nat. Mater.* **12**, 611–616 (2013).
2. S. O. Valenzuela, M. Tinkham, Electrical detection of spin currents: The spin-current induced Hall effect (invited). *J. Appl. Phys.* **101**, 09B103 (2007).
3. K. Garello, I. M. Miron, C. O. Avci, F. Freimuth, Y. Mokrousov, S. Blügel, S. Auffret, O. Boulle, G. Gaudin, P. Gambardella, Symmetry and magnitude of spin–orbit torques in ferromagnetic heterostructures. *Nat. Nanotechnol.* **8**, 587–593 (2013).
4. J. Kim, J. Sinha, M. Hayashi, M. Yamanouchi, S. Fukami, T. Suzuki, S. Mitani, H. Ohno, Layer thickness dependence of the current-induced effective field vector in Ta|CoFeB|MgO. *Nat. Mater.* **12**, 240–245 (2013).
5. Y.-W. Oh, S.-h. C. Baek, Y. M. Kim, H. Y. Lee, K.-D. Lee, C. Yang, E. Park, K.-S. Lee, K.-W. Kim, G. Go, J.-R. Jeong, B.-C. Min, H.-W. Lee, K.-J. Lee, B.-G. Park, Field-free switching of perpendicular magnetization through spin–orbit torque in antiferromagnet/ferromagnet/oxide structures. *Nat. Nanotechnol.* **11**, 878–884 (2016).
6. A. Manchón, I. M. Miron, T. Jungwirth, J. Sinova, J. Zelezný, A. Thiaville, K. Garello, P. Gambardella, Current-induced spin-orbit torques in ferromagnetic and antiferromagnetic systems. arXiv:1801.09636 [cond-mat.mes-hall] (29 January 2018).
7. M. Baumgartner, K. Garello, J. Mendil, C. O. Avci, E. Grimaldi, C. Murer, J. Feng, M. Gabureac, C. Stamm, Y. Acremann, S. Finizio, S. Wintz, J. Raabe, P. Gambardella, Spatially and time-resolved magnetization dynamics driven by spin–orbit torques. *Nat. Nanotechnol.* **12**, 980–986 (2017).
8. A. R. Mellnik, J. S. Lee, A. Richardella, J. L. Grab, P. J. Mintun, M. H. Fischer, A. Vaezi, A. Manchon, E.-A. Kim, N. Samarth, D. C. Ralph, Spin-transfer torque generated by a topological insulator. *Nature* **511**, 449–451 (2014).
9. Y. Fan, P. Upadhyaya, X. Kou, M. Lang, S. Takei, Z. Wang, J. Tang, L. He, L.-T. Chang, M. Montazeri, G. Yu, W. Jiang, T. Nie, R. N. Schwartz, Y. Tserkovnyak, K. L. Wang, Magnetization switching through giant spin–orbit torque in a magnetically doped topological insulator heterostructure. *Nat. Mater.* **13**, 699–704 (2014).
10. W. Zhang, W. Han, X. Jiang, S.-H. Yang, S. S. P. Parkin, Role of transparency of platinum–ferromagnet interfaces in determining the intrinsic magnitude of the spin Hall effect. *Nat. Phys.* **11**, 496–502 (2015).
11. L. Liu, C.-F. Pai, Y. Li, H. W. Tseng, D. C. Ralph, R. A. Buhrman, Spin-torque switching with the giant spin Hall effect of tantalum. *Science* **336**, 555–558 (2012).
12. C.-F. Pai, L. Liu, Y. Li, H. W. Tseng, D. C. Ralph, R. A. Buhrman, Spin transfer torque devices utilizing the giant spin Hall effect of tungsten. *Appl. Phys. Lett.* **101**, 122404 (2012).
13. Y. Niimi, Y. Kawanishi, D. H. Wei, C. Deranlot, H. X. Yang, M. Chshiev, T. Valet, A. Fert, Y. Otani, Giant spin Hall effect induced by skew scattering from bismuth impurities inside thin film CuBi alloys. *Phys. Rev. Lett.* **109**, 156602 (2012).
14. Y. Ou, D. C. Ralph, R. A. Buhrman, Strong enhancement of the spin Hall effect by spin fluctuations near the curie point of Fe_xPt_{1-x} alloys. *Phys. Rev. Lett.* **120**, 097203 (2018).
15. W. Zhang, W. Han, S.-H. Yang, Y. Sun, Y. Zhang, B. Yan, S. S. P. Parkin, Giant facet-dependent spin-orbit torque and spin Hall conductivity in the triangular antiferromagnet $IrMn_3$. *Sci. Adv.* **2**, e1600759 (2016).
16. V. Tshitoyan, C. Ciccarelli, A. P. Mihai, M. Ali, A. C. Irvine, T. A. Moore, T. Jungwirth, A. J. Ferguson, Electrical manipulation of ferromagnetic NiFe by antiferromagnetic IrMn. *Phys. Rev. B* **92**, 214406 (2015).
17. W. Zhang, M. B. Jungfleisch, W. Jiang, J. E. Pearson, A. Hoffmann, F. Freimuth, Y. Mokrousov, Spin Hall effects in metallic antiferromagnets. *Phys. Rev. Lett.* **113**, 196602 (2014).
18. J. B. S. Mendes, R. O. Cunha, O. Alves Santos, P. R. T. Ribeiro, F. L. A. Machado, R. L. Rodríguez-Suárez, A. Azevedo, S. M. Rezende, Large inverse spin Hall effect in the antiferromagnetic metal $Ir_{20}Mn_{80}$. *Phys. Rev. B* **89**, 140406(R) (2014).
19. W. Zhang, M. B. Jungfleisch, F. Freimuth, W. Jiang, J. Sklenar, J. E. Pearson, J. B. Ketterson, Y. Mokrousov, A. Hoffmann, All-electrical manipulation of magnetization dynamics in a ferromagnet by antiferromagnets with anisotropic spin Hall effects. *Phys. Rev. B* **92**, 144405 (2015).
20. H. Saglam, J. C. Rojas-Sanchez, S. Petit, M. Hehn, W. Zhang, J. E. Pearson, S. Mangin, A. Hoffmann, Independence of spin-orbit torques from the exchange bias direction in $Ni_{81}Fe_{19}$/IrMn bilayers. *Phys. Rev. B* **98**, 094407 (2018).
21. A. Kohn, A. Kovacs, R. Fan, G. J. McIntyre, R. C. C. Ward, J. P. Goff, The antiferromagnetic structures of $IrMn_3$ and their influence on exchange-bias. *Sci. Rep.* **3**, 2412 (2013).
22. E. Krén, G. Kádár, L. Pál, J. Sólyom, P. Szabó, T. Tarnóczi, Magnetic structures and exchange interactions in the Mn-Pt system. *Phys. Rev.* **171**, 574–585 (1968).
23. C. S. Severin, C. W. Chen, C. Stassis, Neutron-diffraction study of the magnetic structure of MnPt alloys. *J. Appl. Phys.* **50**, 4259–4262 (1979).
24. H. Hama, R. Motomura, T. Shinozaki, Y. Tsunoda, Spin–flip transition of $L1_0$-type MnPt alloy single crystal studied by neutron scattering. *J. Phys. Condens. Matter* **19**, 176228 (2007).
25. A. C. Larson, R. B. Von Dreele, "General Structure Analysis System (GSAS)" (Report LAUR 86-748, Los Alamos National Laboratory, 1994).
26. Y. F. Ding, J. S. Chen, E. Liu, C. J. Sun, G. M. Chow, Effect of lattice mismatch on chemical ordering of epitaxial $L1_0$ FePt films. *J. Appl. Phys.* **97**, 10H303 (2005).
27. L. Liu, T. Moriyama, D. C. Ralph, R. A. Buhrman, Spin-torque ferromagnetic resonance induced by the spin Hall effect. *Phys. Rev. Lett.* **106**, 036601 (2011).
28. K.-W. Kim, K.-J. Lee, J. Sinova, H.-W. Lee, M. D. Stiles, Spin-orbit torques from interfacial spin-orbit coupling for various interfaces. *Phys. Rev. B* **96**, 104438 (2017).
29. P. M. Haney, H.-W. Lee, K.-J. Lee, A. Manchon, M. D. Stiles, Current induced torques and interfacial spin-orbit coupling: Semiclassical modeling. *Phys. Rev. B* **87**, 174411 (2013).
30. J. Zhou, S. Chen, W. Lin, Q. Qin, L. Liu, S. He, J. Chen, Effects of field annealing on Gilbert damping of polycrystalline CoFe thin films. *J. Magn. Magn. Mater.* **441**, 264–270 (2017).
31. A. Okada, S. He, B. Gu, S. Kanai, A. Soumyanarayanan, S. T. Lim, M. Tran, M. Mori, S. Maekawa, F. Matsukura, H. Ohno, C. Panagopoulos, Magnetization dynamics and its scattering mechanism in thin CoFeB films with interfacial anisotropy. *Proc. Natl. Acad. Sci. U.S.A.* **114**, 3815–3820 (2017).
32. J.-C. Rojas-Sánchez, N. Reyren, P. Laczkowski, W. Savero, J.-P. Attané, C. Deranlot, M. Jamet, J.-M. George, L. Vila, H. Jaffrès, Spin pumping and inverse spin Hall effect in platinum: The essential role of spin-memory loss at metallic interfaces. *Phys. Rev. Lett.* **112**, 106602 (2014).
33. Y. Liu, Z. Yuan, R. J. H. Wesselink, A. A. Starikov, P. J. Kelly, Interface enhancement of Gilbert damping from first principles. *Phys. Rev. Lett.* **113**, 207202 (2014).
34. W. Zhang, K. M. Krishnan, Epitaxial exchange-bias systems: From fundamentals to future spin-orbitronics. *Mater. Sci. Eng. R Rep.* **105**, 1–20 (2016).
35. M. J. Pechan, D. Bennett, N. Teng, Induced anisotropy and positive exchange bias: A temperature, angular, and cooling field study by ferromagnetic resonance. *Phys. Rev. B* **65**, 064410 (2002).
36. C.-F. Pai, Y. Ou, L. H. Vilela-Leão, D. C. Ralph, R. A. Buhrman, Dependence of the efficiency of spin Hall torque on the transparency of Pt/ferromagnetic layer interfaces. *Phys. Rev. B* **92**, 064426 (2015).
37. K. Dolui, B. K. Nikolić, Spin-memory loss due to spin-orbit coupling at ferromagnet/heavy-metal interfaces: Ab initio spin-density matrix approach. *Phys. Rev. B* **96**, 220403(R) (2017).
38. H. Nakayama, M. Althammer, Y.-T. Chen, K. Uchida, Y. Kajiwara, D. Kikuchi, T. Ohtani, S. Geprägs, M. Opel, S. Takahashi, R. Gross, G. E. W. Bauer, S. T. B. Goennenwein, E. Saitoh, Spin Hall magnetoresistance induced by a nonequilibrium proximity effect. *Phys. Rev. Lett.* **110**, 206601 (2013).
39. J. Železný, H. Gao, K. Výborný, J. Zemen, J. Mašek, A. Manchon, J. Wunderlich, Relativistic Néel-order fields induced by electrical current in antiferromagnets. *Phys. Rev. Lett.* **113**, 157201 (2014).
40. D. MacNeill, G. M. Stiehl, M. H. D. Guimaraes, R. A. Buhrman, J. Park, D. C. Ralph, Control of spin–orbit torques through crystal symmetry in WTe_2/ferromagnet bilayers. *Nat. Phys.* **13**, 300–305 (2017).
41. A. Kumar, S. Akansel, H. Stopfel, M. Fazlali, J. Åkerman, R. Brucas, P. Svedlindh, Spin transfer torque ferromagnetic resonance induced spin pumping in the Fe/Pd bilayer system. *Phys. Rev. B* **95**, 064406 (2017).
42. X. Tao, Q. Liu, B. Miao, R. Yu, Z. Feng, L. Sun, B. You, J. Du, K. Chen, S. Zhang, L. Zhang, Z. Yuan, D. Wu, H. Ding, Self-consistent determination of spin Hall angle and spin diffusion length in Pt and Pd: The role of the interface spin loss. *Sci. Adv.* **4**, eaat1670 (2018).
43. R. Ramaswamy, Y. Wang, M. Elyasi, M. Motapothula, T. Venkatesan, X. Qiu, H. Yang, Extrinsic spin Hall effect in $Cu_{1-x}Pt_x$. *Phys. Rev. Appl.* **8**, 024034 (2017).
44. K. Koepernik, H. Eschrig, Full-potential nonorthogonal local-orbital minimum-basis band-structure scheme. *Phys. Rev. B* **59**, 1743–1757 (1999).
45. I. Opahle, K. Koepernik, H. Eschrig, Full-potential band-structure calculation of iron pyrite. *Phys. Rev. B* **60**, 14035–14041 (1999).
46. J. P. Perdew, K. Burke, M. Ernzerhof, Generalized gradient approximation made simple. *Phys. Rev. Lett.* **77**, 3865–3868 (1996).
47. J. Sinova, D. Culcer, Q. Niu, N. A. Sinitsyn, T. Jungwirth, A. H. MacDonald, Universal intrinsic spin Hall effect. *Phys. Rev. Lett.* **92**, 126603 (2004).

48. K. Fritz, S. Wimmer, H. Ebert, M. Meinert, Large spin Hall effect in an amorphous binary alloy. *Phys. Rev. B* **98**, 094433 (2018).
49. C. O. Avci, K. Garello, M. Gabureac, A. Ghosh, A. Fuhrer, S. F. Alvarado, P. Gambardella, Interplay of spin-orbit torque and thermoelectric effects in ferromagnet/normal-metal bilayers. *Phys. Rev. B* **90**, 224427 (2014).

Acknowledgments: We thank S. K. He for the advice on ST-FMR system design and measurement. We thank C. Sun for the constructive discussion on SOT and structures of IrMn. **Funding:** This project was partially supported by the National Key Research and Development Program of China (title: Nonvolatile and programmable spin logics based on magnetic heterostructures; grant no. 2017YFA0206200) for the device microfabrications. We would like to acknowledge SSLS for providing the facility necessary for conducting the research. P.Y. was supported by SSLS via NUS Core Support C-380-003-003-001. The Laboratory is a National Research Infrastructure under the National Research Foundation (NRF) Singapore. A portion of this research used resources at the High Flux Isotope Reactor and Spallation Neutron Source, U.S. DOE Office of Science User Facilities operated by the Oak Ridge National Laboratory. J.C. is a member of Singapore Spintronics Consortium (SG-SPIN). This research was supported by Singapore National Research Foundation under CRP award no. NRF-CRP10-2012-02 and IIP award no. NRF-IIP001-001. B.Y. acknowledges the financial support by a research grant from the Benoziyo Endowment Fund for the Advancement of Science. This manuscript has been authored by UT-Battelle, LLC under contract no. DE-AC05-00OR22725 with the U.S. Department of Energy. The U.S. government retains and the publisher, by accepting the article for publication, acknowledges that the U.S. government retains a nonexclusive, paid-up, irrevocable, and worldwide license to publish or reproduce the published form of this manuscript, or allow others to do so, for U.S. government purposes. The Department of Energy will provide public access to these results of federally sponsored research in accordance with the DOE Public Access Plan (http://energy.gov/downloads/doe-public-access-plan). **Author contributions:** J.C. conceived the study and supervised the experiment. J.Z. built the ST-FMR measurement system, deposited thin-film samples, and performed ST-FMR measurement. X.W., J.Y., and H.Y.Y. fabricated microdevices. Y.L., T.H., and M.M. performed neutron diffraction experiment. H.F. and B.Y. carried out ab initio calculation. J.D. and P.Y. measured XRD and RSM. L.L. and W.L. measured electrical conductivity. S.C. deposited part of the thin-film samples. S.A. performed GSAS refinement. X.S. performed measurement on HRTEM. J.Z., B.Y., X.H., and J.C. wrote the manuscript. All authors helped to revise the manuscript and contributed to the final version. **Competing interest:** The authors declare that they have no competing interests. **Data and materials availability:** All data needed to evaluate the conclusions in the paper are present in the paper and/or the Supplementary Materials. Additional data related to this paper may be requested from the authors.

Submitted 9 November 2018
Accepted 1 April 2019
Published 10 May 2019
10.1126/sciadv.aau6696

Citation: J. Zhou, X. Wang, Y. Liu, J. Yu, H. Fu, L. Liu, S. Chen, J. Deng, W. Lin, X. Shu, H. Y. Yoong, T. Hong, M. Matsuda, P. Yang, S. Adams, B. Yan, X. Han, J. Chen, Large spin-orbit torque efficiency enhanced by magnetic structure of collinear antiferromagnet IrMn. *Sci. Adv.* **5**, eaau6696 (2019).